Maximizing MeV x-ray dose in relativistic laser-solid interactions

Kyle G. Miller , ^{1,*} Dean R. Rusby , ² Andreas J. Kemp, ² Scott C. Wilks, ² and Warren B. Mori

¹Departments of Physics and Astronomy and of Electrical and Computer Engineering,

University of California, Los Angeles, California 90095, USA

²Lawrence Livermore National Laboratory, Livermore, California 94551, USA

(Received 15 February 2022; revised 27 October 2022; accepted 16 February 2023; published 23 March 2023)

Bremsstrahlung x rays generated in laser-solid interactions can be used as light sources for high-energy-density science. We present electron and x-ray spectra from multidimensional kinetic simulations with varying laser pulse intensity and duration at fixed energy of 200 J. A phenomenological model for the transition from superponderomotive to ponderomotive temperatures is described, yielding a temperature scaling that depends on pulse duration and density scale length. The shortest pulses create low-divergence electron beams before self-generated magnetic fields evolve, yielding 1–5-MeV forward-going x rays containing \sim 0.5% of the laser energy.

DOI: 10.1103/PhysRevResearch.5.L012044

The interaction of a high-intensity laser pulse with a solid target produces a high forward flux of multi-MeV electrons through a variety of physical mechanisms [1–6]. The "hot" electrons can produce bremsstrahlung x rays [7,8], which are of interest for a variety of applications [9–11]. Work has been devoted to optimizing bremsstrahlung production and controlling its directionality, including the use of preformed plasmas [5,8,12], advanced nanowires [13,14], and cone-shaped targets [15,16]. In addition, laser absorption has been shown to rise with increased laser intensity and oblique incidence [17,18]. Particle energies greater than predicted by traditional scaling laws have been observed for long-pulse lasers [19] and subpicosecond laser pulses coupled with submillimeter near-critical-density foams [20]. Certain schemes using PW-class laser systems can produce brilliant, collimated multi-MeV photons [21–23]; however, the techniques discussed herein are scalable to kilojoule laser systems and generate pointlike x-ray sources that are more ideal for highenergy-density imaging and industrial radiography.

In this Letter, we present particle-in-cell (PIC) simulation results on relativistic laser-solid interactions where the laser pulse amplitude and duration are varied with energy held constant. Recent computational techniques [24,25] detailed hereafter are employed that allow for large-scale (hundreds of micrometers) and long-time (tens of picoseconds) simulations of such interactions. Electron spectra and beam profiles determined from PIC simulations are used as input for Monte Carlo simulations to calculate x-ray spectra, and a clear maximum in 1–5-MeV x-ray dose is found as a function of laser intensity.

Published by the American Physical Society under the terms of the Creative Commons Attribution 4.0 International license. Further distribution of this work must maintain attribution to the author(s) and the published article's title, journal citation, and DOI.

All PIC simulations are performed with OSIRIS [26]. The density rises from near zero to $10n_c$ from x = -27.6 to 0 µm in an exponential profile of the form $10n_c e^{x/L_0}$, where the scale length L_0 is 3 µm, and n_c is the critical density; the density remains $10n_c$ for positive x. We use two-dimensional (2D) Cartesian simulations where the plasma is 240-µm wide in y and extends to 150 μ m in x at the right edge with electrons and ions (with a charge-to-mass ratio of $e/2m_p$, where e is electron charge and m_p is proton mass) initialized at a temperature of 0.1 keV. Open and thermal boundary conditions are used for fields and particles, respectively, except for an open particle boundary condition at the left wall. A diffraction-limited Gaussian laser with spot size, w_0 , 30 μm is launched from left to right in the \hat{x} direction with a focus at the critical surface, where the Rayleigh length is $\pi w_0^2/\lambda$ and λ is the laser wavelength. Although each PIC simulation corresponds to a family of cases with identical normalized parameters, we give physical units corresponding to $\lambda = 1 \,\mu\text{m}$. We vary the amplitude and duration of the laser, keeping the product $a_0^2\tau$ constant at 10 ps, where $a_0 \simeq 8.6 \times 10^{-10} \sqrt{I_0 \text{ (W/cm}^2)} \lambda \text{ (}\mu\text{m)}$ is the normalized vector potential for vacuum intensity I_0 , and τ is the full width at half maximum (FWHM) of intensity. The lowestand highest-intensity cases have $(a_0, \tau) = (0.58, 30 \text{ ps})$ and (31.6, 0.01 ps), respectively, with energy 200 J for all cases an energy achievable by many picosecond-class laser systems. The laser profile is Gaussian in the transverse direction and is a polynomial function temporally [27]. Cell sizes are $0.4 c/\omega_0$ in each direction, where ω_0 is the laser frequency. The time step is $0.282\omega_0^{-1}$, and simulations end 2 ps after the laser is extinguished. A limited set of simulations is also performed with cells of size $0.2c/\omega_0$ ($a_0 = 5.77, 20$), with a peak density of $30n_c$ and cell size $0.2c/\omega_0$ ($a_0 = 25$), and with collisions ($a_0 = 25$) to ensure that results do not depend on the resolution and are not subject to relativistic transparency or collisional effects. Figure 1 shows the electron density, laser envelope, and forward electron energy flux [defined as $Q_x = \int v_x(\gamma - 1) m_e c^2 F(\vec{x}, \vec{p}) d\vec{p}$ for the plasma distribution

^{*}kmill@lle.rochester.edu

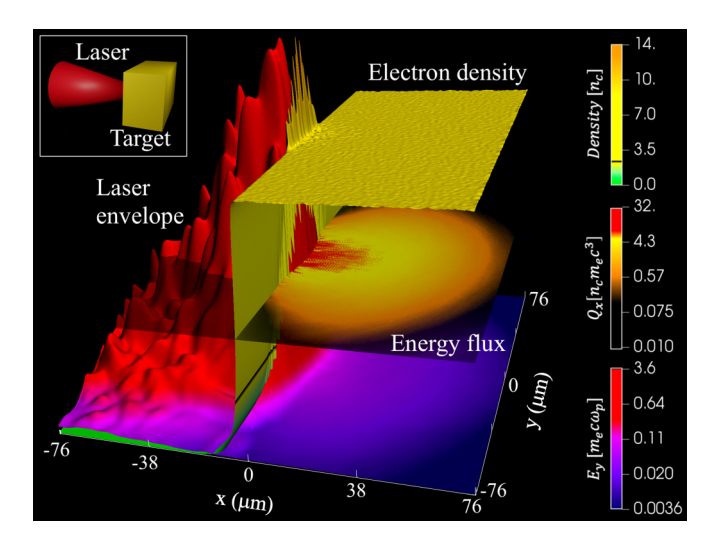


FIG. 1. Electron density, transverse laser field envelope, and forward electron energy flux for a laser with $(a_0, \tau) = (1.83, 3 \text{ ps})$ and w_0 of 30 μ m near when the peak of the laser pulse reaches the critical surface. Quantities are spatially averaged for visualization.

function F] for a simulation with $(a_0, \tau) = (1.83, 3 \text{ ps})$. The plasma density sharply increases near the laser axis, and the laser is observed to penetrate slightly into the overdense region where the electron energy flux is greatest.

To make such long-time simulations possible, we employ some unique PIC techniques. Electrons (ions) are simulated with 64 (16) particles per cell, but in order to avoid numerical stopping of energetic particles from the enhanced wakes of macroparticles [24], fast electrons ($\gamma > 1.5$) are split into 64 smaller particles. To prevent hot-electron refluxing from simulation boundaries, extended particle absorbers [25] are employed over the regions $|y| \ge 110$ and $x \ge 130$ µm to gradually stop energetic particles without unphysically large electric-field growth. Low-energy particles with small charge in the absorbing regions are later combined to reduce computational load. The left vacuum boundary in x is located so as to be causally separated from the vacuum-plasma interface (varied based on simulation time). Last, to avoid numerical grid heating and to further reduce the enhanced wakes, we use cubic particle shapes.

The Monte Carlo simulation package GEANT4 [28] is used to compute the energy and number of bremsstrahlung x rays generated by the high-energy electrons from the PIC simulations. The GEANT4 code is capable of simulating the bremsstrahlung radiation from individual particles, although it neglects self-consistent electromagnetic fields and other collective effects. First, the forward-going high-energy electron spectra (i.e., electrons with positive v_x 's) are extracted from OSIRIS every 200 time steps over the region 50–57.5 µm in x, and the approximate electron source size and divergence angle are estimated. Although these electrons follow nearly straight-line trajectories from the plasma interface to this region within OSIRIS, in reality bremsstrahlung emission will begin immediately within the target. Thus, we then inject an electron beam with the measured source characteristics (i.e., spectrum, size, and angle at the plasma interface) directly into 500 µm of tungsten using GEANT4, with hundreds of

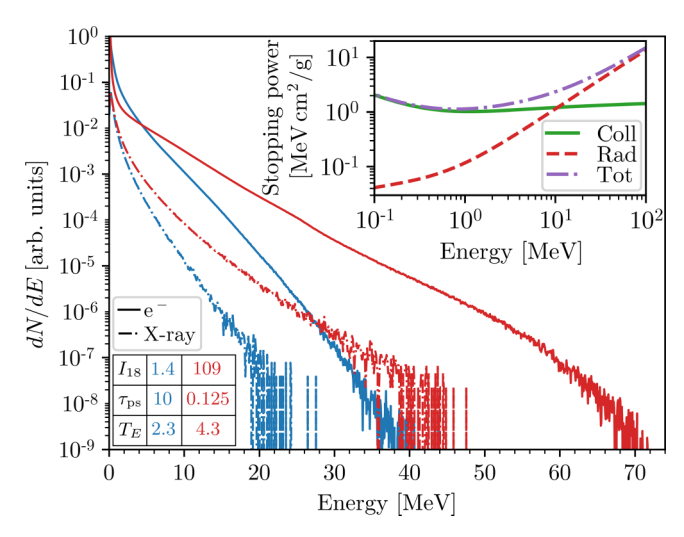


FIG. 2. Time-integrated electron and resulting photon spectra for two simulations at identical laser pulse energy (laser intensity, FWHM, and electron temperature labeled in units of $10^{18} \, \text{W/cm}^2$, picoseconds, and MeV, respectively). The inset shows the stopping power (collisional, radiative, and total) of tungsten as a function of electron energy.

equisized energy bins between 0.2–100 MeV. Finally, the x-ray spectra are time integrated as a function of emitted angle and weighted according to the corresponding electron dose.

Figure 2 shows the cumulative forward-going OSIRIS electron spectra for two simulations. The inset shows the stopping power of tungsten as a function of electron energy. Dashed-dot lines show the resulting x-ray spectra computed from GEANT4 and collected over all angles. Although the low-intensity (blue) simulation in Fig. 2 gives nearly twice the number of 1–5-MeV electrons as the high-intensity (orange) simulation, the large stopping power of many-MeV electrons results in more x rays of all energies for the high-intensity simulation with a higher electron temperature.

Aggregate data from our sequence of PIC simulations are shown in Fig. 3. In (a), we show the amplitude A and electron temperature T_E of exponential fits performed over 3-30 MeV. The generation of energetic electrons is a complicated process that has been described by many differing scaling laws and analyses [29]. Rather than compare to this Letter, we also show the ponderomotive temperature scaling [2,30] as a reference point, which goes as T_{Pond} = $m_e c^2 (\sqrt{1 + a_0^2/2} - 1)$ for a linearly polarized laser. The ponderomotive scaling indicates that T_E scales with the laser field for $a_0 \gg 1$; this corresponds to the work performed on an electron after it moves a single laser wavelength, which is more characteristic of the high-intensity laser pulses. However, at low intensity (long duration), the plasma expands, and electrons in the low-density region can repeatedly and stochastically interact with the incident and reflected laser pulses over a long distance, generating electrons with temperatures and energies much larger than the ponderomotive potential [31–35].

Insight into how electron spectra are generated and how they scale with intensity can be found by looking at the tracks

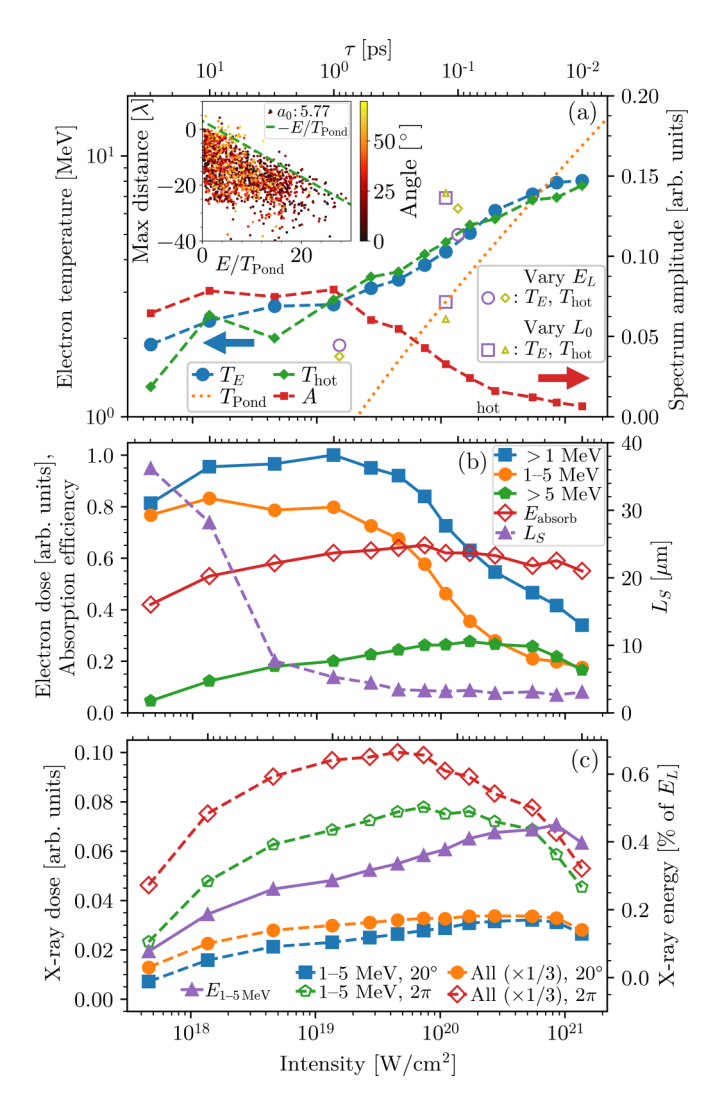


FIG. 3. (a) Scaling of hot electron temperature with laser intensity at constant energy. The A and T_E values result from an exponential fit Ae^{-E/T_E} to the simulated cumulative forward electron spectra, where E is energy. The inset shows the farthest distance tracked particles extend away from the constant-density region as a function of their final energy within in the target for a single simulation, colored by absolute angle from the x axis in the target. (b) Electron dose (normalized to the largest value), fraction of the laser energy absorbed E_{absorb} and plasma scale length L_S after half of the laser pulse duration. (c) X-ray dose as a function of intensity with the same normalization as in (b), collected within a forward cone of 20° aperture (blue/orange) and at all angles (green/red). X-ray counts over all energies are scaled by 1/3 for visibility. Also shown is the fraction of laser energy contained in the forward cone of 1–5-MeV x rays.

of individual electrons. The inset to Fig. 3(a) shows the distribution of the farthest distance 1500 tracked electrons travel into the low-density region as a function of their final energy after being accelerated into the target for the simulation with $(a_0, \tau) = (5.77, 300 \text{ fs})$. On this scale, the initial density ramp begins at -27.6λ and becomes constant at 0λ , although the constant-density shelf is pushed into the target a distance of 8λ near the laser axis late in the simulation. For a given energy, there is a distribution of distances that electrons have

penetrated into the low-density region, leading to an electron temperature T_E . However, to obtain an energy of NT_{Pond} , an electron must interact with the laser for, at least, a distance of $N\lambda$ as seen by the dashed line with a slope of negative unity. Electrons are colored by the angle of their trajectory with respect to the x axis when propagating through the target. Although no trend in angular distribution is observed with distance traveled into the low-density plasma, we see that more energetic electrons have, on average, a lower divergence. We will discuss this shortly.

To better predict electron temperature based on the laser and plasma conditions, we argue that the temperature should depend on both the laser duration τ and the average scale length of the simulated plasma L_S . Under the assumptions that the plasma density upramp is purely exponential (of the form e^{x/L_S} in the negative x half-space) and that an electron a distance d away from the critical interface can attain a maximum energy of $E_{\text{max}} = \frac{d}{\lambda} T_{\text{Pond}}$ [as shown in the Fig. 3(a) inset], we show in Appendix A that the electron temperature scales as

$$T_{\text{hot}} = \left(\frac{1}{E_D} + \frac{1}{\bar{L}T_{\text{Pond}}}\right)^{-1}, \quad E_D \approx \frac{m_e c^2 a_0}{2\sqrt{\pi}} \sqrt{\frac{\tau}{T_0}}, \quad (1)$$

where T_0 is the laser period and $\bar{L} \equiv \mathrm{Max}[\frac{L_S}{\lambda}, 1]$. The parameter E_D gives the magnitude of energy diffusion during the acceleration process (i.e., electrons gain a spread of energies up to E_{max} over one laser cycle); it is constant with laser energy and emerges from $\lim_{\bar{L}T_{\mathrm{Pond}}\to\infty} T_{\mathrm{hot}} = E_D$. The value of E_D can be estimated either via Eq. (1) or as the maximum electron temperature observed from simulations with increasingly large a_0 at constant laser energy (see Appendix A), e.g., the temperature at the highest intensity in Fig. 3(a). In both cases, the value is close to $E_D \approx 10$ MeV for our parameters. We set $\bar{L} \geqslant 1$ so that the temperature approaches T_{Pond} for very short scale lengths [1,36,37].

The scale temperature from Eq. (1) with $E_D = 10 \text{ MeV}$ and L_S taken from Fig. 3(b) is shown to give good agreement with the simulated temperature data in Fig. 3(a). Additional simulations are performed with laser energy E_L varied by a factor of 3 and with initial density scale length L_0 varied by a factor of 10 as pictured by the hollow symbols in Fig. 3(a), and reasonable agreement is also observed [Eq. (1) is used to estimate E_D].

In Fig. 3(b), we report the time-integrated forward-going electron dose for three energy ranges (normalized to the largest value shown), along with the fraction of the laser energy absorbed by forward-going electrons and the plasma scale length after half of the laser pulse duration. The dose of 1–5-MeV electrons is largest for the low-intensity laser pulses, whereas the number of >5-MeV electrons steadily increases with intensity. However, we observe that the total energy absorbed into hot electrons from the laser remains close to 60% for all but the lowest-intensity cases. The near-constant absorption poses the question of how to best maximize x-ray production given the observed electron doses.

From the simulated electron spectra and beam profiles, we then compute the observed x-ray spectra using GEANT4

as described previously. In Fig. 3(c), we plot the x-ray dose collected both inside a forward cone of 20° aperture as well as over all angles. The x-ray dose in the energy range of 1–5 MeV is shown alongside the dose over all energies, and the latter is scaled by 1/3 for visibility. For context, computing the x-ray spectra using only the amplitude and temperature fits shown in Fig. 3(a) reproduces the 1–5-MeV x-ray dose to 1% accuracy for most cases. As mentioned previously, a higher-resolution simulation performed with $a_0 = 25$ and peak density $30n_c$ exhibited a change of less than 3% in the 1–5-MeV x-ray dose, which gives confidence in the chosen simulation parameters. The forward-going x-ray dose very closely follows the >5-MeV electron dose shown in Fig. 3(b), peaking somewhere between 10²⁰ and 10²¹ W/cm². The 1–5-MeV x-ray dose peaks near 5×10^{20} W/cm², demonstrating that high-energy (>5-MeV) electrons are desirable for producing few-MeV x rays. For the best case, the total energy contained in the forward-going 1-5-MeV x rays is 0.45% of the laser energy, and 1.3% of the laser energy is contained in forward-going x rays of >1-MeV energy; the total photon number is more than 10^{12} .

The electron-beam divergence is relatively constant with laser intensity, although it drops by roughly a factor of 2 at the highest intensity (see Appendix B). Both the electron and the x-ray angular distributions are shown in Fig. 4(a) for two cases with, and the higher-intensity case exhibits a much narrower spread in angle. We observe in Fig. 4(b) that for the case with $(a_0, \tau) = (25, 16 \text{ fs})$, a self-generated magnetic field forms at the plasma interface due to the electron temperature anisotropy [38–42], which, in turn, increases the electron divergence angle. The simulated growth time for modes with $k_{\rm v} > 0.06k_{\rm p} \approx 1.25 \ \mu {\rm m}^{-1}$ is $\Gamma^{-1} \approx 4.3 \ {\rm fs}$, or $\Gamma \approx 0.04\omega_{\rm p}$, and the most unstable wave numbers are in the range of $0.05k_p \lesssim k_y \lesssim 0.25k_p$. These dynamics are confirmed with three-dimensional (3D), uniform, and periodic simulations using the early-time electron distribution as detailed in the Appendix C. In Fig. 4, we show (c)–(e) the transverse Fourier transform of the magnetic field that is time integrated over one laser period, (f)–(h) the same magnetic field in real space, and (i)–(k) the forward electron energy flux at three different times for the $(a_0, \tau) = (25, 16 \text{ fs})$ case, where t_0 is the time when the first energetic electron bunch nears the constant-density interface. Two planar groups of electrons are observed at the right edge of (k), which correlate to the first two spikes in $\frac{dQ}{dt}$ in (b); these electrons are emitted before the magnetic fields form, and as such have a much smaller divergence angle than the rest of the electrons. Thus, for laser pulses with duration on the order of the self-generated magnetic-field growth time, the electron divergence can be lower, resulting in more forwardgoing x rays.

In conclusion, we have studied the generation of MeV x rays from intense laser-solid interactions using a combination of large-scale, two-dimensional OSIRIS PIC and GEANT4 Monte Carlo simulations. Keeping the laser pulse energy constant at 200 J for a 30- μ m spot size, we find that the optimal forward dose of 1–5–MeV x rays results from a laser intensity near 5×10^{20} W/cm² and duration of 25 fs, yielding more than 10^{12} photons that contain 0.45% of the laser energy (1.3% of laser energy in >1-MeV x rays). A scaling of the energetic electron temperature based on phenomenological

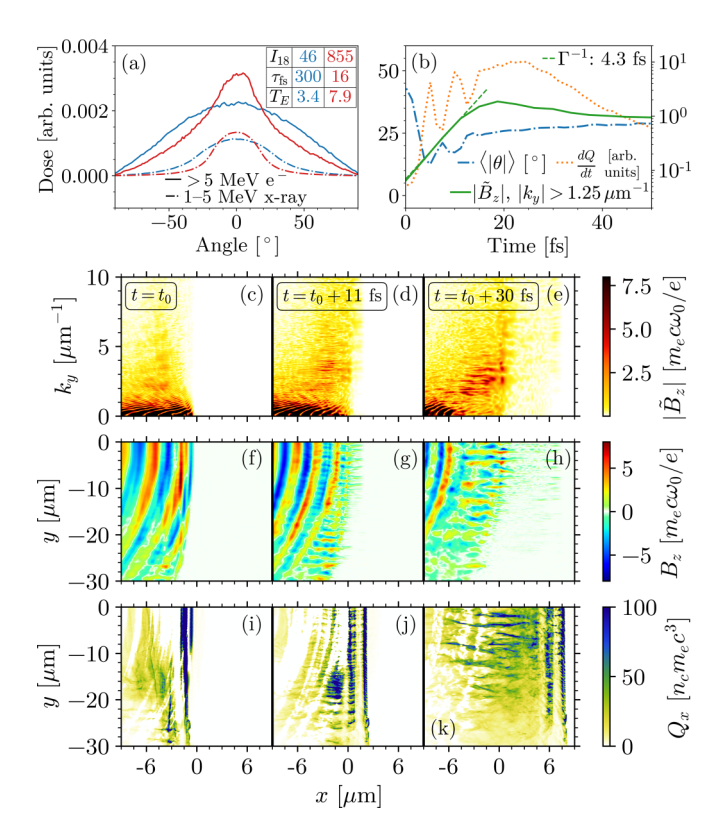


FIG. 4. (a) Electron and x-ray angles of emission for two cases of laser intensity. For the $(a_0, \tau) = (25, 16\text{-fs})$ case we then show (b) average emission angle for >1-MeV electrons $\langle |\theta| \rangle$, flux of electron beam charge $\frac{dQ}{dt}$, and amplitude of the transverse Fourier transform of the magnetic field $|\tilde{B}_z|$ for modes with $|k_y| > 1.25 \ \mu\text{m}^{-1}$. In (c)–(k), we show $|\tilde{B}_z|$, B_z , and the forward electron energy flux Q_x for three different times, where t_0 is the time when the first energetic electron bunch nears the constant-density interface.

arguments is given in Eq. (1) and includes a dependence on laser duration and density scale length. The formation of self-generated magnetic fields near the critical-density surface over only a few laser periods increases the electron-beam divergence, leading to decreased forward-going x-ray emission for all but the shortest of pulses. Simulation results for a wide range of laser pulse parameters show that for fixed laser energy, high-intensity (and short-duration) laser pulses generally produce more few-MeV x rays than do low-intensity pulses due to the formation of electron beams with high temperature and low divergence.

We acknowledge useful conversations with J. P. Palastro. This work was performed under the auspices of the U.S. DOE by Lawrence Livermore National Laboratory (LLNL) under Contract No. DE-AC52-07NA27344 and funded by the LLNL LDRD Program with tracking code 19-SI-002 under Contract No. B635445. Additional support was given by DOE Grants No. DE-SC0019010 and No. DE-NA0003842 and NSF Grant No. 2108970. Release under the IM:LLNL-JRNL-831656-DRAFT. Computer simulations were performed with a Grand Challenge allocation at the Livermore Computing Center and on NERSC's Cori cluster (Accounts No. m1157 and No. m3013).

APPENDIX A: PHENOMENOLOGICAL ARGUMENT FOR THE ELECTRON TEMPERATURE SCALING

To derive an expression for the electron temperature, we assume that the plasma density upramp over the duration of the laser-solid interaction can be approximated as $n_c e^{x/L_s}$, where n_c is the critical density (located at x=0 in this case), L_S is an average or typical scale length, and the low-density plasma is located in the x<0 half-space. We also assume that an electron will gain a maximum energy of T_{Pond} from interacting with a single cycle of the laser, i.e., that an electron initially located at position x can be accelerated to the critical surface with a maximum final energy of $E_{max}(x) = \frac{|x|}{\lambda} T_{Pond}$. Finally, we assume that the probability of the actual energy gain of such an electron decreases exponentially as a function of energy. Our position-energy distribution function then takes the form

$$P(x, E) = Ae^{x/L_S - E/E_D} \mathcal{H}(E_{\text{max}}[x] - E),$$
 (A1)

where A is a normalization constant, E is the electron energy, E_D is some scale energy that dictates the efficiency of the energy conversion process, and $\mathcal{H}(E)$ is the Heaviside step function. We can integrate away position to obtain the temperature distribution function, or

$$P(E) = \int_{-\infty}^{0} dx A e^{x/L_S - E/E_D} \mathcal{H}\left(\frac{|x|}{\lambda} T_{\text{Pond}} - E\right)$$
$$= AL_S e^{-E(\frac{1}{E_D} + \frac{\lambda}{L_S T_{\text{Pond}}})}. \tag{A2}$$

The scale temperature T_{hot} is then observed to be

$$T_{\text{hot}} = \left(\frac{1}{E_D} + \frac{1}{\bar{L}T_{\text{Pond}}}\right)^{-1},\tag{A3}$$

where $\bar{L} \equiv \text{Max}[\frac{L_S}{\lambda}, 1]$. We define \bar{L} to have a minimum value of 1 because we desire that the scale temperature approach T_{Pond} for plasmas with very short scale lengths (i.e., less than a laser wavelength).

In the limit that $\bar{L}T_{Pond} \rightarrow \infty$, we have that $T_{hot} \rightarrow E_D$. Thus, E_D can be thought of as an upper limit for the attainable temperature of a given problem with a very large scale length or very intense laser pulse. However, this upper limit could depend on the laser spot size and duration or plasma temperature. One way to obtain this value in practice would be to simulate a laser-solid problem of interest, but with the laser pulse compressed to a very short duration (with equal energy).

Another way to estimate E_D is by relating it to the electron energy spread due to interaction with the laser. Over one laser wavelength, the laser can provide a kick K to the momentum p of a given electron with amplitude $\Delta p = K = T_{\rm Pond}/c$. However, the change in momentum could be less than this or in a direction that opposes the electron motion. Thus, we expect a distribution of electron energies due to the stochastic acceleration process. The quasilinear approximation to the diffusion coefficient in momentum space D for an integrable system receiving periodic kicks of amplitude

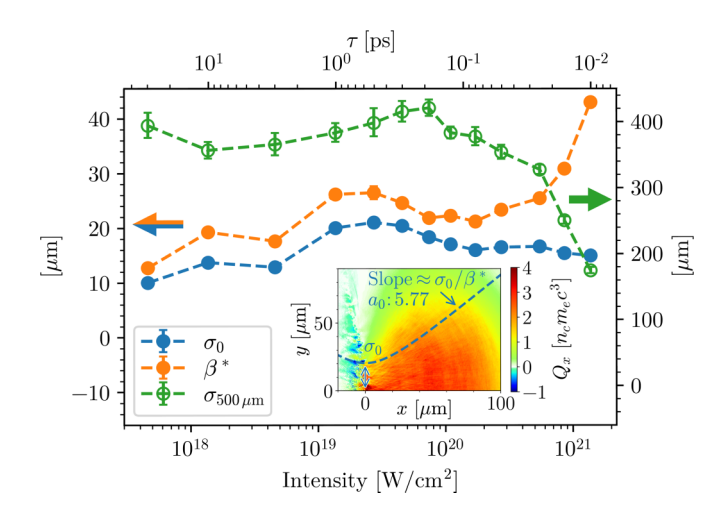


FIG. 5. Beam parameters at the source and spot size evaluated at 500 μ m for the hot electrons with respect to laser intensity, where $\sigma(x) = \sigma_0 \sqrt{1 + (x/\beta^*)^2}$. The inset shows example fitted beam parameters.

K is $D \approx K^2/4 = T_{\rm Pond}^2/4c^2$, and the resulting momentum distribution function f(p,n) after n kicks is [43]

$$f(p,n) \approx \frac{1}{\sqrt{2\pi nD}} \exp\left(-\frac{p^2}{2nD}\right).$$
 (A4)

For values of $a_0 \gg 1$, we have that $T_{\rm Pond} \approx m_e c^2 a_0 / \sqrt{2}$, and that $E \approx |p|c$. Thus, to find the energy spread, we seek to calculate $\langle E \rangle = \langle |p| \rangle c$, where angle brackets denote a time average. Integrating Eq. (A4) to find the average momentum

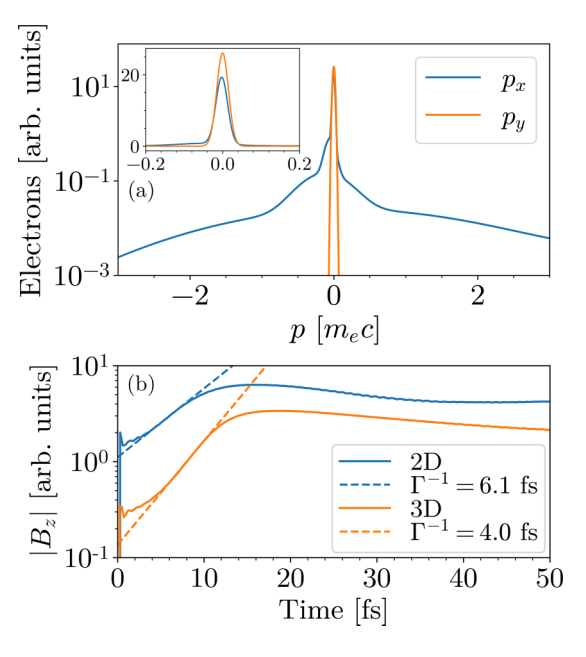


FIG. 6. (a) Approximation to the electron momentum distribution for the case with $(a_0, \tau) = (25, 16 \text{ fs})$, just before the magnetic fields begin to develop. The inset shows the same data on a linear scale. (b) Growth of the self-generated magnetic fields for simulations of a periodic box in 2D and 3D, respectively.

yields $\langle |p| \rangle = \sqrt{2nD/\pi}$ or that

$$E_D \equiv \langle E \rangle = T_{\text{Pond}} \sqrt{\frac{n}{2\pi}} \approx \frac{m_e c^2 a_0}{2\sqrt{\pi}} \sqrt{\frac{\tau}{T_0}},$$
 (A5)

where we have used $n = \tau/T_0$ with τ as the laser pulse duration and T_0 as the laser period.

APPENDIX B: ELECTRON-BEAM CHARACTERIZATION

To accurately determine the x-ray production using such a large variety of pulse amplitudes, we must first characterize any differences in the angular spread of the electron beam. To accomplish this, we track a 10-µm slice of electrons generated from the peak of each laser pulse as it travels through and spreads into the target from 0 to 130 µm. Fitting the forward energy flux near the vacuum interface to a Gaussian profile in the transverse direction $(e^{-y^2/2\sigma_0^2})$, we compute the initial beam width σ_0 . Assuming a beam evolution of $\sigma(x) =$ $\sigma_0 \sqrt{1 + (x/\beta^*)^2}$, we then make a fit for β^* using the energy flux as a function of x. Although such a fit is most useful when the incoming energy is carried by a well-defined beam with low-energy spread and high energy, it still provides a useful characterization for the beam. We show the parameter fits in Fig. 5 along with the spot size evaluated at 500 μ m, $\sigma_{500 \,\mu m}$. The electron beam becomes significantly less divergent for the high-intensity short-duration laser pulses, which is favorable for forward x-ray emission.

APPENDIX C: SELF-GENERATED MAGNETIC FIELDS DUE TO ELECTRON TEMPERATURE ANISOTROPY

The self-generated magnetic fields we observe are due to an electron temperature anisotropy as high-energy electrons propagate into the target [38–40]. Other works have explored the dependence of these fields on laser and plasma parameters [41,42]. Here, to confirm the magnetic-field generation mechanism, we initialize a plasma in a periodic box with fixed ions and an electron momentum distribution similar to that found in the full-scale simulation with $(a_0, \tau) = (25, 16 \text{ fs})$ just before the magnetic fields begin to develop. The distribution is shown in Fig. 6(a), and the overall distribution is separable in p_x and p_y . We use cell sizes of $0.4 c/\omega_0$. In Fig. 6(b), we plot the spatially integrated absolute value of the magnetic field $|B_z|$ as a function of time for the 2D and 3D cases. The results are nearly identical when using mobile ions, and simulations with finer resolution show a similar transverse structure in the saturated state. The growth times in each case are comparable to that observed in the fullscale simulation $\Gamma^{-1} = 4.3$ fs, indicating that the observed self-generated magnetic fields are indeed produced from the momentum anisotropy.

- [11] C. M. Brenner, S. R. Mirfayzi, D. R. Rusby, C. Armstrong, A. Alejo, L. A. Wilson, R. Clarke, H. Ahmed, N. M. H. Butler, D. Haddock, A. Higginson, A. McClymont, C. Murphy, M. Notley, P. Oliver, R. Allott, C. Hernandez-Gomez, S. Kar, P. McKenna, and D. Neely, Laser-driven x-ray and neutron source development for industrial applications of plasma accelerators, Plasma Phys. Controlled Fusion 58, 014039 (2016).
- [12] O. Culfa, G. J. Tallents, A. K. Rossall, E. Wagenaars, C. P. Ridgers, C. D. Murphy, R. J. Dance, R. J. Gray, P. McKenna, C. D. R. Brown, S. F. James, D. J. Hoarty, N. Booth, A. P. L. Robinson, K. L. Lancaster, S. A. Pikuz, A. Y. Faenov, T. Kampfer, K. S. Schulze, I. Uschmann, and N. C. Woolsey, Plasma scale-length effects on electron energy spectra in high-irradiance laser plasmas, Phys. Rev. E 93, 043201 (2016).

S. C. Wilks, W. L. Kruer, M. Tabak, and A. B. Langdon, Absorption of Ultra-Intense Laser Pulses, Phys. Rev. Lett. 69, 1383 (1992).

^[2] G. Malka and J. L. Miquel, Experimental Confirmation of Ponderomotive-Force Electrons Produced by an Ultrarelativistic Laser Pulse on a Solid Target, Phys. Rev. Lett. 77, 75 (1996).

^[3] S. C. Wilks and W. L. Kruer, Absorption of ultrashort, ultraintense laser light by solids and overdense plasmas, IEEE J. Quantum Electron. 33, 1954 (1997).

^[4] A. Pukhov and J. Meyer-ter Vehn, Relativistic laser-plasma interaction by multi-dimensional particle-in-cell simulations, Phys. Plasmas 5, 1880 (1998).

^[5] M. I. K. Santala, E. Clark, I. Watts, F. N. Beg, M. Tatarakis, M. Zepf, K. Krushelnick, A. E. Dangor, T. McCanny, I. Spencer, R. P. Singhal, K. W. D. Ledingham, S. C. Wilks, A. C. Machacek, J. S. Wark, R. Allott, R. J. Clarke, and P. A. Norreys, Effect of the Plasma Density Scale Length on the Direction of Fast Electrons in Relativistic Laser-Solid Interactions, Phys. Rev. Lett. 84, 1459 (2000).

^[6] J. May, J. Tonge, F. Fiuza, R. A. Fonseca, L. O. Silva, C. Ren, and W. B. Mori, Mechanism of generating fast electrons by an intense laser at a steep overdense interface, Phys. Rev. E 84, 025401(R) (2011).

^[7] M. D. Perry, J. A. Sefcik, T. Cowan, S. Hatchett, A. Hunt, M. Moran, D. Pennington, R. Snavely, and S. C. Wilks, Hard x-ray production from high intensity laser solid interactions (invited), Rev. Sci. Instrum. 70, 265 (1999).

^[8] C. Courtois, A. Compant La Fontaine, O. Landoas, G. Lidove, V. Méot, P. Morel, R. Nuter, E. Lefebvre, A. Boscheron, J. Grenier, M. M. Aléonard, M. Gerbaux, F. Gobet, F. Hannachi, G. Malka, J. N. Scheurer, and M. Tarisien, Effect of plasma

density scale length on the properties of bremsstrahlung x-ray sources created by picosecond laser pulses, Phys. Plasmas **16**, 013105 (2009).

^[9] J. C. Kieffer, A. Krol, Z. Jiang, C. C. Chamberlain, E. Scalzetti, and Z. Ichalalene, Future of laser-based X-ray sources for medical imaging, Appl. Phys. B: Lasers Opt. 74, s75 (2002).

^[10] D. R. Rusby, C. M. Brenner, C. Armstrong, L. A. Wilson, R. Clarke, A. Alejo, H. Ahmed, N. M. H. Butler, D. Haddock, A. Higginson, A. McClymont, S. R. Mirfayzi, C. Murphy, M. Notley, P. Oliver, R. Allott, C. Hernandez-Gomez, S. Kar, P. McKenna, and D. Neely, Pulsed x-ray imaging of high-density objects using a ten picosecond high-intensity laser driver, in *Emerging Imaging and Sensing Technologies*, edited by K. L Lewis and R. C. Hollins (SPIE, Bellingham, WA, 2016), Vol. 9992, pp. 61–68, doi:10.1117/12.2241776.

- [13] S. Jiang, A. G. Krygier, D. W. Schumacher, K. U. Akli, and R. R. Freeman, Enhancing Bremsstrahlung production from ultraintense laser-solid interactions with front surface structures, Eur. Phys. J. D 68, 283 (2014).
- [14] T. Ebert, N. W. Neumann, L. N. K. Döhl, J. Jarrett, C. Baird, R. Heathcote, M. Hesse, A. Hughes, P. McKenna, D. Neely, D. Rusby, G. Schaumann, C. Spindloe, A. Tebartz, N. Woolsey, and M. Roth, Enhanced brightness of a laser-driven x-ray and particle source by microstructured surfaces of silicon targets, Phys. Plasmas 27, 043106 (2020).
- [15] S. A. Gaillard, T. Kluge, K. A. Flippo, M. Bussmann, B. Gall, T. Lockard, M. Geissel, D. T. Offermann, M. Schollmeier, Y. Sentoku, and T. E. Cowan, Increased laser-accelerated proton energies via direct laser-light-pressure acceleration of electrons in microcone targets, Phys. Plasmas 18, 056710 (2011).
- [16] T. Kluge, S. A. Gaillard, K. A. Flippo, T. Burris-Mog, W. Enghardt, B. Gall, M. Geissel, A. Helm, S. D. Kraft, T. Lockard, J. Metzkes, D. T. Offermann, M. Schollmeier, U. Schramm, K. Zeil, M. Bussmann, and T. E. Cowan, High proton energies from cone targets: Electron acceleration mechanisms, New J. Phys. 14, 023038 (2012).
- [17] Y. Ping, R. Shepherd, B. F. Lasinski, M. Tabak, H. Chen, H. K. Chung, K. B. Fournier, S. B. Hansen, A. Kemp, D. A. Liedahl, K. Widmann, S. C. Wilks, W. Rozmus, and M. Sherlock, Absorption of Short Laser Pulses on Solid Targets in the Ultrarelativistic Regime, Phys. Rev. Lett. 100, 085004 (2008).
- [18] J. R. Davies, Laser absorption by overdense plasmas in the relativistic regime, Plasma Phys. Controlled Fusion 51, 014006 (2009).
- [19] R. A. Simpson, G. G. Scott, D. Mariscal, D. Rusby, P. M. King, E. Grace, A. Aghedo, I. Pagano, M. Sinclair, C. Armstrong, M. J. E. Manuel, A. Haid, K. Flippo, L. Winslow, M. Gatu-Johnson, J. A. Frenje, D. Neely, S. Kerr, G. J. Williams, S. Andrews, R. Cauble, K. Charron, R. Costa, B. Fischer, S. Maricle, B. Stuart, F. Albert, N. Lemos, A. Mackinnon, A. MacPhee, A. Pak, and T. Ma, Scaling of laser-driven electron and proton acceleration as a function of laser pulse duration, energy, and intensity in the multi-picosecond regime, Phys. Plasmas 28, 013108 (2021).
- [20] M. M. Günther, O. N. Rosmej, P. Tavana, M. Gyrdymov, A. Skobliakov, A. Kantsyrev, S. Zähter, N. G. Borisenko, A. Pukhov, and N. E. Andreev, Forward-looking insights in laser-generated ultra-intense γ-ray and neutron sources for nuclear application and science, Nat. Commun. 13, 170 (2022).
- [21] D. J. Stark, T. Toncian, and A. V. Arefiev, Enhanced Multi-MeV Photon Emission by a Laser-Driven Electron Beam in a Self-Generated Magnetic Field, Phys. Rev. Lett. 116, 185003 (2016).
- [22] T. Wang, X. Ribeyre, Z. Gong, O. Jansen, E. d'Humières, D. Stutman, T. Toncian, and A. Arefiev, Power Scaling for Collimated γ -Ray Beams Generated by Structured Laser-Irradiated Targets and Its Application to Two-Photon Pair Production, Phys. Rev. Appl. **13**, 054024 (2020).
- [23] X.-L. Zhu, M. Chen, S.-M. Weng, T.-P. Yu, W.-M. Wang, F. He, Z.-M. Sheng, P. McKenna, D. A. Jaroszynski, and J. Zhang, Extremely brilliant GeV *γ*-rays from a two-stage laser-plasma accelerator, Sci. Adv. **6**, aaz7240 (2020).

- [24] J. May, J. Tonge, I. Ellis, W. B. Mori, F. Fiuza, R. A. Fonseca, L. O. Silva, and C. Ren, Enhanced stopping of macro-particles in particle-in-cell simulations, Phys. Plasmas **21**, 052703 (2014).
- [25] K. G. Miller, J. May, F. Fiuza, and W. B. Mori, Extended particle absorber for efficient modeling of intense laser–solid interactions, Phys. Plasmas 28, 112702 (2021).
- [26] R. A. Fonseca, L. O. Silva, F. S. Tsung, V. K. Decyk, W. Lu, C. Ren, W. B. Mori, S. Deng, S. Lee, T. Katsouleas, and J. C. Adam, OSIRIS: A three-dimensional, fully relativistic particle in cell code for modeling plasma based accelerators, in *Computational Science—ICCS 2002: International Conference Amsterdam*, 2002 Proceedings, Part III, edited by P. M. A. Sloot, A. G. Hoekstra, C. J. K. Tan, and J. J. Dongarra, Lecture Notes in Computer Science, Vol. 2331 (Springer, Berlin/Heidelberg, 2002), pp. 342–351, doi: 10.1007/3-540-47789-6_36.
- [27] F. S. Tsung, W. Lu, M. Tzoufras, W. B. Mori, C. Joshi, J. M. Vieira, L. O. Silva, and R. A. Fonseca, Simulation of monoenergetic electron generation via laser wakefield accelerators for 5–25TW lasers, Phys. Plasmas 13, 056708 (2006).
- [28] S. Agostinelli, J. Allison, K. Amako, J. Apostolakis, H. Araujo, P. Arce, M. Asai, D. Axen, S. Banerjee, G. Barrand, F. Behner, L. Bellagamba, J. Boudreau, L. Broglia, A. Brunengo, H. Burkhardt, S. Chauvie, J. Chuma, R. Chytracek, G. Cooperman, G. Cosmo, P. Degtvarenko, A. Dell'Acqua, G. Depaola, D. Dietrich, R. Enami, A. Feliciello, C. Ferguson, H. Fesefeldt, G. Folger, F. Foppiano, A. Forti, S. Garelli, S. Giani, R. Giannitrapani, D. Gibin, J. J. Gómez Cadenas, I. González, G. Gracia Abril, G. Greeniaus, W. Greiner, V. Grichine, A. Grossheim, S. Guatelli, P. Gumplinger, R. Hamatsu, K. Hashimoto, H. Hasui, A. Heikkinen, A. Howard, V. Ivanchenko, A. Johnson, F. W. Jones, J. Kallenbach, N. Kanaya, M. Kawabata, Y. Kawabata, M. Kawaguti, S. Kelner, P. Kent, A. Kimura, T. Kodama, R. Kokoulin, M. Kossov, H. Kurashige, E. Lamanna, T. Lampén, V. Lara, V. Lefebure, F. Lei, M. Liendl, W. Lockman, F. Longo, S. Magni, M. Maire, E. Medernach, K. Minamimoto, P. Mora de Freitas, Y. Morita, K. Murakami, M. Nagamatu, R. Nartallo, P. Nieminen, T. Nishimura, K. Ohtsubo, M. Okamura, S. O'Neale, Y. Oohata, K. Paech, J. Perl, A. Pfeiffer, M. G. Pia, F. Ranjard, A. Rybin, S. Sadilov, E. Di Salvo, G. Santin, T. Sasaki, N. Savvas, Y. Sawada, S. Scherer, S. Sei, V. Sirotenko, D. Smith, N. Starkov, H. Stoecker, J. Sulkimo, M. Takahata, S. Tanaka, E. Tcherniaev, E. Safai Tehrani, M. Tropeano, P. Truscott, H. Uno, L. Urban, P. Urban, M. Verderi, A. Walkden, W. Wander, H. Weber, J. P. Wellisch, T. Wenaus, D. C. Williams, D. Wright, T. Yamada, H. Yoshida, and D. Zschiesche, Geant4—a simulation toolkit, Nucl. Instrum. Methods Phys. Res., Sect. A 506, 250
- [29] A. Compant La Fontaine, Photon dose produced by a high-intensity laser on a solid target, J. Phys. D: Appl. Phys. 47, 325201 (2014).
- [30] S. C. Wilks, Simulations of ultraintense laser–plasma interactions, Phys. Fluids Bs **5**, 2603 (1993).
- [31] J. T. Mendonça and F. Doveil, Stochasticity in plasmas with electromagnetic waves, J. Plasma Phys. 28, 485 (1982).
- [32] D. W. Forslund, J. M. Kindel, W. B. Mori, C. Joshi, and J. M. Dawson, Two-Dimensional Simulations of Single-Frequency and Beat-Wave Laser-Plasma Heating, Phys. Rev. Lett. 54, 558 (1985).

- [33] J. Meyer-ter Vehn and Z. M. Sheng, On electron acceleration by intense laser pulses in the presence of a stochastic field, Phys. Plasmas **6**, 641 (1999).
- [34] A. Sorokovikova, A. V. Arefiev, C. McGuffey, B. Qiao, A. P. L. Robinson, M. S. Wei, H. S. McLean, and F. N. Beg, Generation of Superponderomotive Electrons in Multipicosecond Interactions of Kilojoule Laser Beams with Solid-Density Plasmas, Phys. Rev. Lett. 116, 155001 (2016).
- [35] A. J. Kemp and S. C. Wilks, Direct electron acceleration in multi-kilojoule, multi-picosecond laser pulses, Phys. Plasmas **27**, 103106 (2020).
- [36] B. F. Lasinski, A. B. Langdon, S. P. Hatchett, M. H. Key, and M. Tabak, Particle-in-cell simulations of ultra intense laser pulses propagating through overdense plasma for fastignitor and radiography applications, Phys. Plasmas 6, 2041 (1999).
- [37] J. Tonge, J. May, W. B. Mori, F. Fiuza, S. F. Martins, R. A. Fonseca, L. O. Silva, and C. Ren, A simulation study of fast ignition with ultrahigh intensity lasers, Phys. Plasmas 16, 056311 (2009).

- [38] M. Tzoufras, C. Ren, F. S. Tsung, J. W. Tonge, W. B. Mori, M. Fiore, R. A. Fonseca, and L. O. Silva, Space-Charge Effects in the Current-Filamentation or Weibel Instability, Phys. Rev. Lett. 96, 105002 (2006).
- [39] M. Tzoufras, C. Ren, F. S. Tsung, J. W. Tonge, W. B. Mori, M. Fiore, R. A. Fonseca, and L. O. Silva, Stability of arbitrary electron velocity distribution functions to electromagnetic modes, Phys. Plasmas 14, 062108 (2007).
- [40] F. Fiuza, R. A. Fonseca, J. Tonge, W. B. Mori, and L. O. Silva, Weibel-Instability-Mediated Collisionless Shocks in the Laboratory with Ultraintense Lasers, Phys. Rev. Lett. 108, 235004 (2012).
- [41] L. G. Huang, H. Takabe, and T. E. Cowan, Maximizing magnetic field generation in high power laser–solid interactions, High Power Laser Sci. Eng. 7, e22 (2019).
- [42] N. Shukla, K. Schoeffler, E. Boella, J. Vieira, R. Fonseca, and L. O. Silva, Interplay between the Weibel instability and the Biermann battery in realistic laser-solid interactions, Phys. Rev. Res. 2, 023129 (2020).
- [43] E. Ott, *Chaos in Dynamical Systems*, 2nd ed. (Cambridge University Press, Cambridge, UK, 2002), Chap. 7, pp. 246–303.